SUPPLEMENTARY MATERIAL

From wood pulp fibers to nanohybrid cellulose microspheres: dissolution, regeneration, functional properties and water remediation

*Joana C. Almeida [a], William M. Facchinatto [a], Vasco Valente [a], Gabriela J. Campos [a], Denis Alikin [b], Andrei Kholkin [b,c], Nicolas Schaeffer [a], Armando J. D. Silvestre [a], Fátima Jesus [d], Joana L. Pereira [d], Adelaide Almeida [d], Carmen S. R. Freire [a], Carla Vilela [a]**

[a] CICECO – Aveiro Institute of Materials, Department of Chemistry, University of Aveiro, 3810-193 Aveiro, Portugal

[b] CICECO – Aveiro Institute of Materials, Department of Physics, University of Aveiro, 3810-193 Aveiro, Portugal

[c] Institute of Solid State Physics, University of Latvia, Riga, LV-1063, Latvia

[d] CESAM – Centre for Environmental and Marine Studies, Department of Biology, University of Aveiro, 3810-193 Aveiro, Portugal

* Corresponding author: cvilela@ua.pt

Contents

I. Cellulose dissolution in an organic electrolyte solution

Wood cellulose fibers were dissolved in an organic electrolyte solution (OES), formed by 1-ethyl-3-methylimidazolium acetate ([Emim][OAc]) and dimethyl sulfoxide (DMSO), during 3 h at 27 °C. Two cellulose concentrations, namely 1.5 wt.% and 3.0 wt.%, and five different mass ratios of [Emim][OAc] and DMSO, namely 50:50, 40:60, 30:70, 25:75 and 20:80, were tested, as outlined in Table S1.

Table S1. List of the studied parameters in the cellulose dissolution assays.

Sample	Mass ratio [Emim][OAc]:DMSO	Molar ratio [Emim][OAc]: DMSO	[Cellulose] (wt.%)	Dissolved (Y/N)*
Cell1.5_50:50	50:50	31:69	1.5	Y
Cell1.5_40:60	40:60	23:77	1.5	Y
Cell1.5_30:70	30:70	16:84	1.5	Y
Cell1.5_25:75	25:75	13:87	1.5	Y
Cell1.5_20:80	20:80	10:90	1.5	N
Cell3_50:50	50:50	31:69	3.0	Y
Cell3_40:60	40:60	23:77	3.0	Y
Cell3_30:70	30:70	16:84	3.0	Y
Cell3_25:75	25:75	13:87	3.0	Y
Cell3_20:80	20:80	10:90	3.0	N

* Y (Yes), N (No)

Fig. S1A displays the visual aspect of the different cellulose solutions using the various mass ratios of [Emim][OAc]:DMSO, whereas Fig. S1B depicts the corresponding optical micrographs of those cellulose solutions. In addition, Fig. S2 shows the attenuated total reflection-Fourier transform Infrared (ATR-FTIR) spectra of the different cellulose solutions, as well as of the corresponding individual components, namely cellulose, [Emim][OAc] and DMSO. Fig. S3 portrays the rheological data of the different cellulose solutions at 27 °C (i.e., temperature at which the dissolution took place). According to these results, both cellulose concentrations, although insoluble in the OES composed of 20:80 mass ratio of [Emim][OAc]:DMSO, originated clear cellulose solutions with [Emim][OAc]:DMSO mass ratios

of 50:50, 40:60, 30:70 and 25:75. These solutions have suitable rheological properties for the dropwise extrusion through a syringe needle aided by a syringe pump.

Fig. S1. (**A**) Digital photographs and (**B**) optical micrographs of the various cellulose solutions (1.5% and 3.0%, w/w) using different mass ratios of [Emim][OAc]:DMSO (50:50, 40:60, 30:70, 25:75 and 20:80).

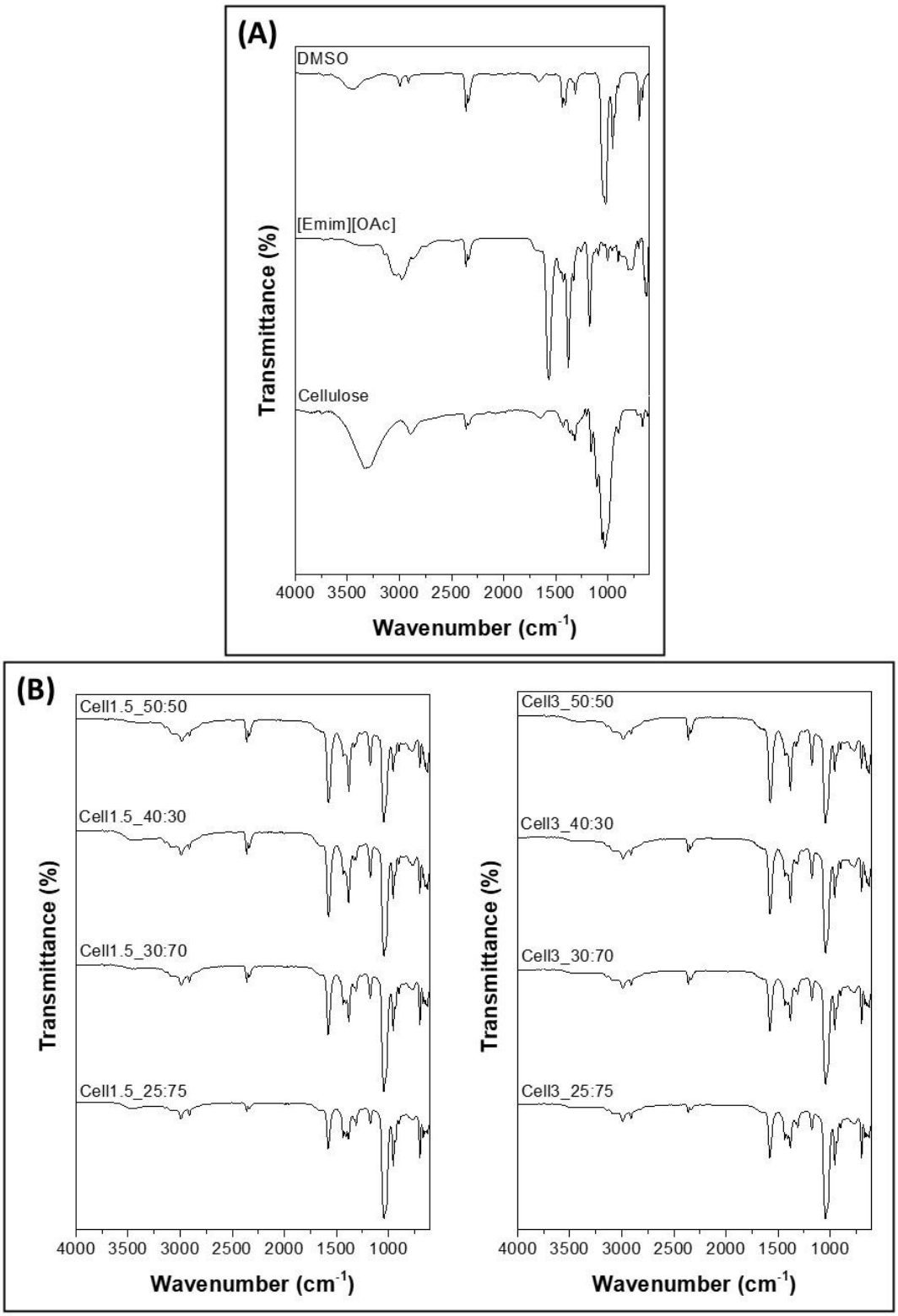

Fig. S2. ATR-FTIR spectra of (**A**) cellulose, [Emim][OAc] and DMSO, and (**B**) the various cellulose solutions (1.5% and 3.0%, w/w) using different mass ratios of [Emim][OAc]:DMSO (50:50, 40:60, 30:70 and 25:75).

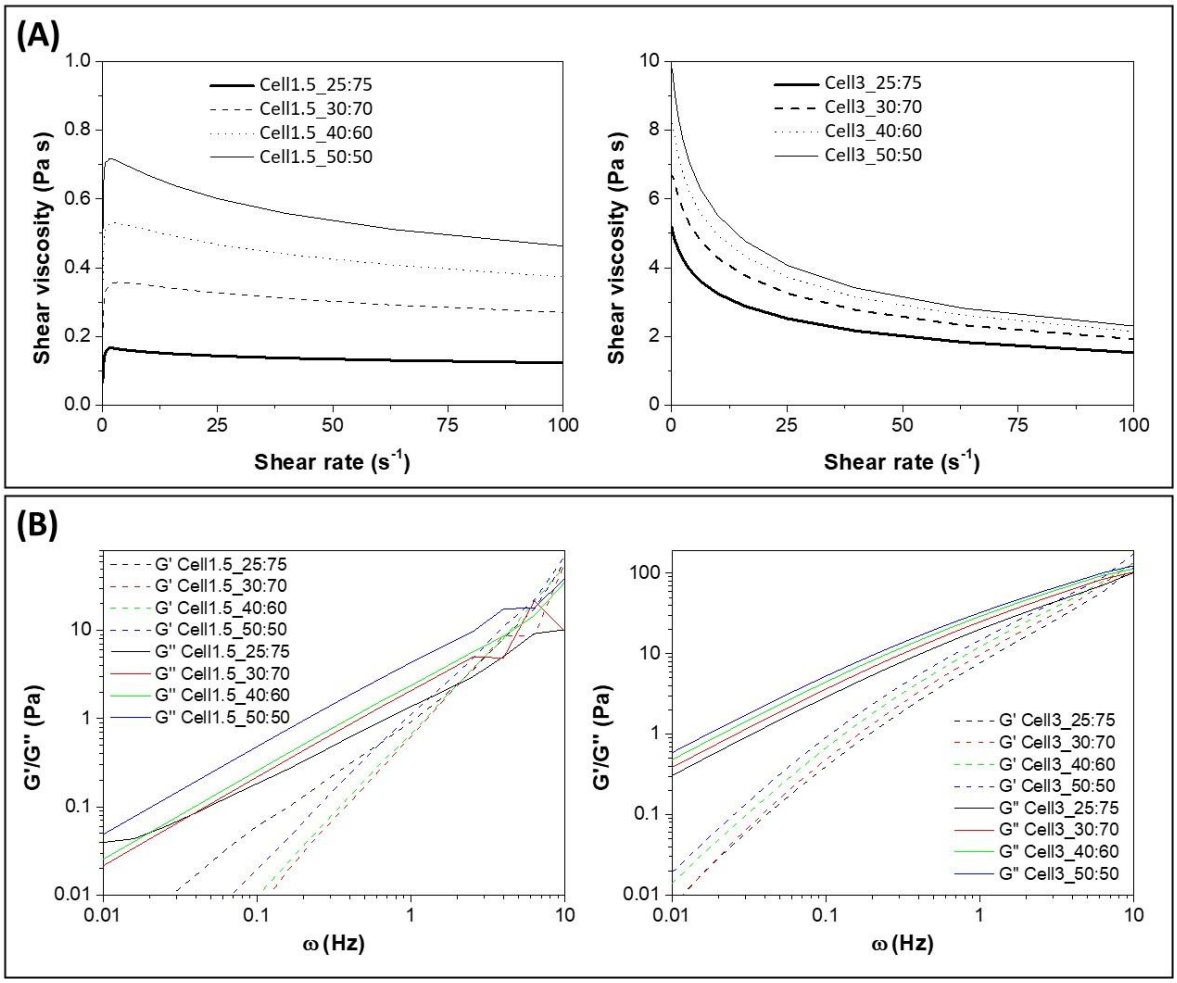

Fig. S3. Rheological data of the various cellulose solutions (1.5% and 3.0%, w/w) using different mass ratios of [Emim][OAc]:DMSO (50:50, 40:60, 30:70 and 25:75): (**A**) viscosity as a function of shear rate, and (**B**) dependence of the elastic modulus (*G*') and viscous modulus (*G*'') on angular frequency.

II. Cellulose regeneration into microspheres

The regeneration of the previously dissolved cellulose into microspheres was tested by adding dropwise the cellulose solution to an anti-solvent, viz., water. Various parameters were verified, namely the concentration (1.5 and 3.0 wt.%) and volume (0.2 and 2.0 mL) of the cellulose solution, the volume (5.0, 10.0 and 20.0 mL) and stirring speed (0, 500 and 1250 rpm) of the anti-solvent, the syringe needle gauge (0.30 and 0.45 mm) and syringe pump flow rate (0.1, 0.2 and 0.5 mL min^{-1}).

Starting with the concentration of the cellulose solution, the regeneration of the various cellulose solutions with a concentration of 1.5 wt.% originated particles that were mostly non-spherical and that collapsed after drying due to the low content of cellulose. Therefore, this

concentration was set aside and all the previously enumerated parameters were tested for the cellulose solutions with a concentration of 3.0 wt.%.

The volume of the antisolvent was also evaluated, as it plays an important role in determining the shape of the resulting particles and preventing the formation of aggregates. In fact, individualized and spherical cellulose particles were only obtained when a larger volume of antisolvent was used. Furthermore, using a higher volume of cellulose solution (2.0 mL) to produce more particles was only achievable when paired with a higher volume of antisolvent (20.0 mL).

In relation to the stirring speed of the antisolvent, the absence of mixing is not advantageous since it leads to the formation of aggregates of non-spherical particles with shape deformities. At 500 rpm, there is also the formation of aggregates of cellulose particles for all cellulose solutions, while at 1250 rpm the particles were spherically shaped without the formation of aggregates.

The syringe needle gauge is another parameter that influences the regeneration of cellulose into microspheres. Depending on the mass ratios of [Emim][OAc]:DMSO (50:50, 40:60, 30:70 and 25:75) used for cellulose dissolution, a considerable strength was required to extrude the more viscous solutions, namely the 50:50 and 40:60. Hence, the use of a 0.45 mm needle gauge facilitates the extrusion of all cellulose solutions, contrary to the 0.30 mm needle gauge.

Regarding the syringe pump flow rate, the regeneration of cellulose was carried out with a solution containing 3.0 wt.% of cellulose dissolved in [Emim][OAc]:DMSO at the various mass ratios (50:50, 40:60, 30:70 and 25:75) and using different flow rates, namely 0.1, 0.2 and 0.5 mL min^{-1} (Fig. S4). For the higher syringe pump flow rates, namely 0.2 and 0.5 mL min^{-1}, the cellulose particles showed some deformities with the formation of tails for all mass ratios of [Emim][OAc]:DMSO, as well the formation of aggregates, particularly for the 50:50 cellulose solution, as illustrated in Fig. S4B,C. When using a flow rate of 0.1 mL min^{-1}, it is evident that the spherical cellulose particles were formed with fewer deformities, principally for the 25:75 mass ratio of [Emim][OAc]:DMSO, as depicted in Fig. S4A.

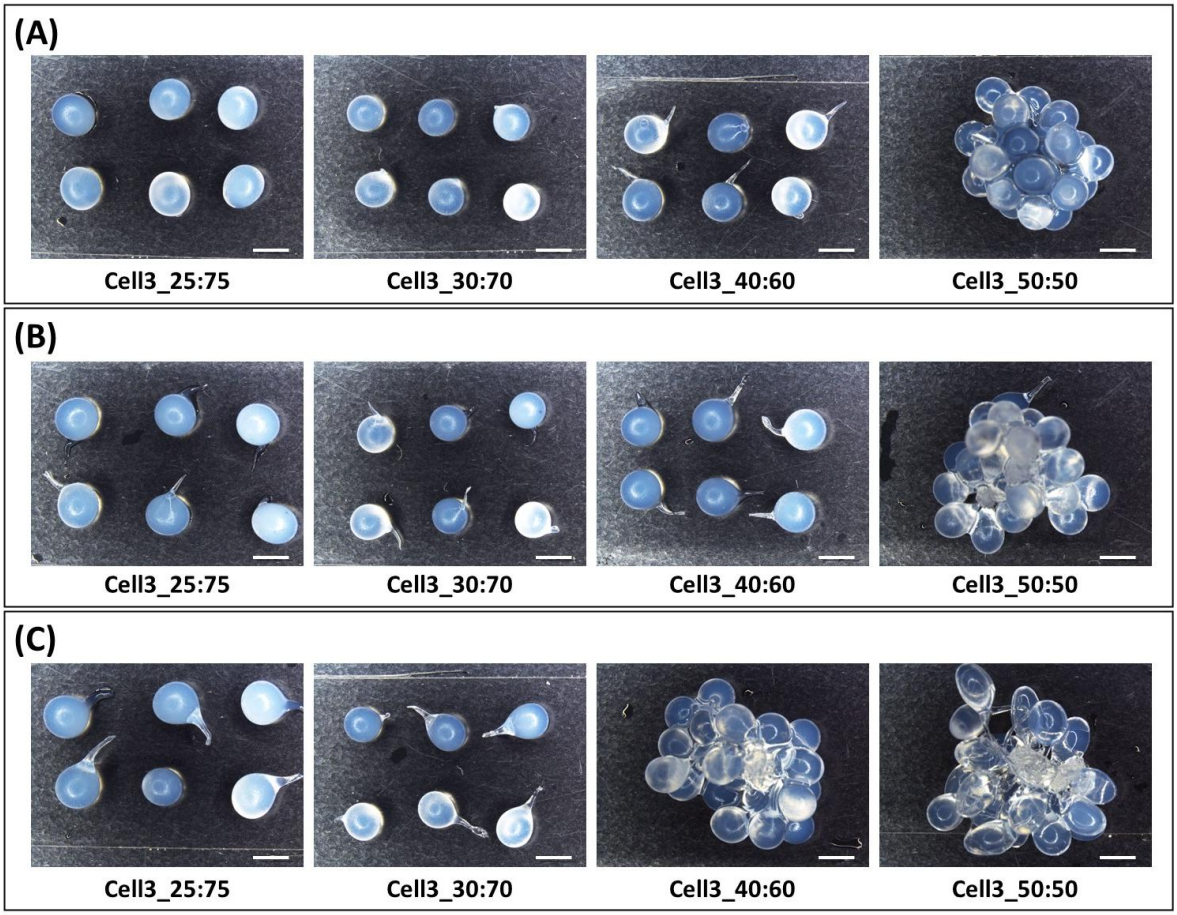

Fig. S4. Optical micrographs (scale bar: 2000 µm) of the cellulose particles prepared with a syringe pump flow rate of (**A**) 0.1 mL min^{-1}, (**B**) 0.2 mL min^{-1}, and (**C**) 0.5 mL min^{-1}, using 2.0 mL of the 3.0 wt.% of cellulose solutions with different mass ratios of [Emim][OAc]:DMSO (25:75, 30:70, 40:60, and 50:50), 20 mL of anti-solvent at 1250 rpm and needle gauge of 0.45 mm.

The drying process is another parameter that must be taken into account, as it affects the shape of the ensuing cellulose particles. In fact, only those dried under ambient conditions generated cellulose particles with a better-defined spherical shape (i.e., cellulose microspheres), as shown in the micrographs of Fig. S5. Therefore, when deem necessary the cellulose microspheres were allowed to dry under ambient conditions, which is the most adequate drying process to obtain these cellulose microspheres.

In sum, the optimized cellulose microspheres were prepared via dissolution of 3 wt.% of the polysaccharide with [Emim][OAc]:DMSO at a mass ratio of 25:75. Then, 2.0 mL of this cellulose solution was extruded through a syringe with a needle gauge of 0.45 mm and a syringe pump flow rate of 0.1 mL min^{-1}, and cellulose was regenerated in 20 mL of anti-solvent stirring at 1250 rpm. Afterwards, the cellulose microspheres were dried under ambient conditions.

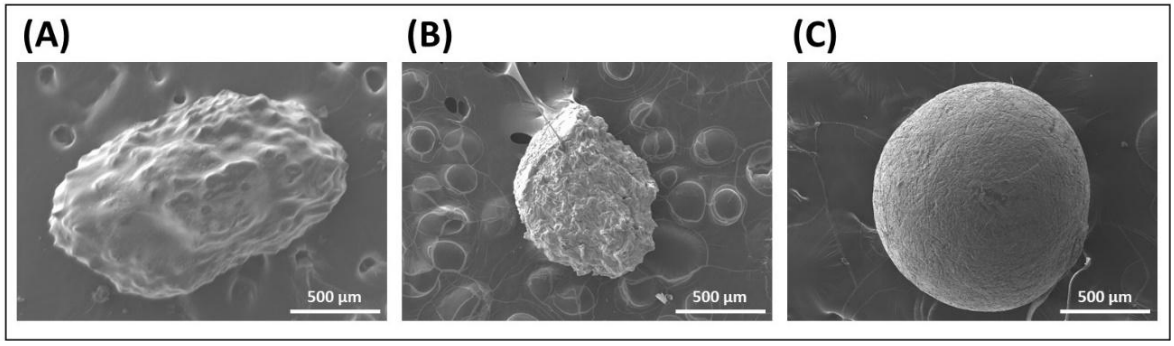

Fig. S5. Scanning electron micrographs of the cellulose particles dried via (**A**) freeze drying, (**B**) oven drying and (**C**) dried under ambient conditions. The cellulose particles were prepared using 2.0 mL of the 3 wt.% of cellulose solution with a mass ratio of 25:75 of [Emim][OAc]:DMSO extruded by a syringe needle gauge of 0.45 mm with a syringe pump flow rate of 0.1 mL min^{-1} to 20 mL of anti-solvent stirring at 1250 rpm.

III. Functionalization of cellulose microspheres with the individual inorganic nanoparticles

The cellulose microspheres were firstly functionalized with the single inorganic nanoparticles (NPs) to select between two assembly methodologies, namely (i) the regeneration of cellulose in the presence of previously synthesized gold (AuNPs), platinum (PtNPs), and iron oxide (Fe_3O_4NPs) nanoparticles, or (ii) the *in situ* synthesis of the AuNPs, PtNPs and Fe_3O_4NPs in the presence of the cellulose microspheres.

III.1. Regeneration of cellulose into microspheres in the presence of inorganic NPs

So first, the three inorganic nanoparticles, namely Au, Pt and Fe_3O_4, were prepared via chemical reduction or co-precipitation of their respective salts. The AuNPs were synthesized via the *in situ* reduction of a gold (III) complex as reported elsewhere [1]. The PtNPs were synthesized by a reduction method with sodium borohydride and trisodium citrate [2]. The Fe_3O_4NPs were prepared by the coprecipitation of Fe(II) and Fe(III) salts in a 1:2 molar ratio, respectively [3].

The color change of the synthesis reactions provided the first indication of the formation of the three types of inorganic nanoparticles. The product of the AuNPs synthesis culminated in a clear pinkish colloidal suspension, while the synthesis of the PtNPs resulted in a clear brownish colloidal suspension (Fig. S6A). It is worth mentioning that this brownish coloration appears immediately after the addition of the colorless reducing agent, thus, indicating the

reduction of the platinum ions and the formation of the PtNPs. The synthesis of the Fe_3O_4NPs generated a dark colloidal suspension (Fig. S6A) [4].

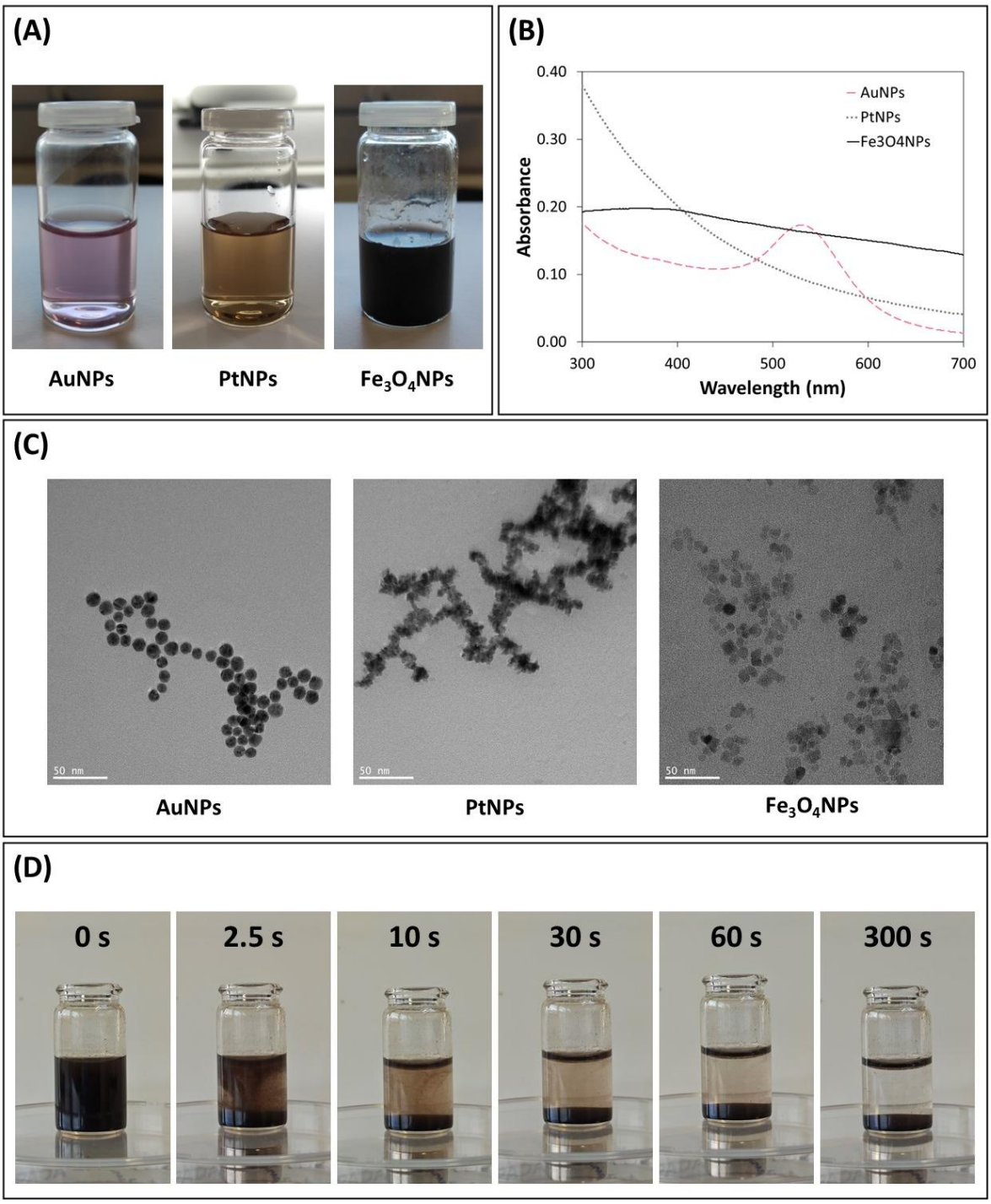

Fig. S6. (**A**) Photographs and (**B**) UV-Vis spectra of the colloidal suspensions of gold nanoparticles (AuNPs), platinum nanoparticles (PtNPs) and iron oxide nanoparticles (Fe_3O_4NPs); and (**C**) TEM micrographs of the inorganic NPs, and (**D**) evolution of the magnetic separation of the colloidal suspension of iron oxide nanoparticles (Fe_3O_4NPs) after exposure to a magnet during 2.5, 10, 30, 60 and 300 s.

The ultraviolet-visible (UV-Vis) spectrum of the AuNPs (Fig. S6B) shows an absorbance maximum centered at around λ = 526 nm, ascribed to the surface plasmon resonance (SPR) band in the visible region [5], whereas the spectra of the PtNPs and Fe_3O_4NPs do not reveal any noticeable absorption bands, in line with data reported elsewhere [4,6].

According to the transmission electron micrographs (Fig. S6C), the three inorganic nanoparticles have sizes in the nanoscale with diameters of 11±1 nm for AuNPs, 5±2 nm for PtNPs and 10±2 nm for Fe_3O_4NPs. These values align with those reported in the respective synthesis methodologies employed [1–3]. Furthermore, the three inorganic NPs have apparent zeta potential values of about –28 mV (in ultrapure water, pH 6.5-7.0, 25 °C), which is consistent with data reported in literature [7–9].

To check the magnetic properties of the Fe_3O_4NPs, a magnet was placed underneath the vial containing the nanoparticles colloidal suspensions. As displayed in Fig. S6D, the Fe_3O_4 NPs were attracted to the magnet and the colloidal suspension started to become transparent with the NPs settling to the bottom of the vial over a short period of time.

After the synthesis and characterization of the inorganic nanoparticles, the first assembly methodology for the cellulose microspheres functionalized with the individual NPs was tested. The regeneration of cellulose in the presence of the previously individually synthesized AuNPs, PtNPs and Fe_3O_4NPs, generated the single hybrids containing 0.23±0.01 mg g^{-1} of Au, 0.65±0.09 mg g^{-1} of Pt and 1.16±0.04 mg g^{-1} of Fe, respectively, as determined by total reflection X-ray fluorescence (TXRF) spectrometry.

III.2. Synthesis of the inorganic NPs in the presence of cellulose microspheres

The second assembly methodology consisted in the *in situ* synthesis of the AuNPs, PtNPs and Fe_3O_4NPs in the presence of the cellulose microspheres. The Cell/AuNPs nanohybrid is composed of 0.37±0.02 mg g^{-1} of Au, the Cell/PtNPs nanohybrid is formed by 1.02±0.02 mg g^{-1} of Pt and the Cell/Fe_3O_4NPs nanohybrid has 63.5±0.6 mg g^{-1} of Fe. So, these results show that the second methodology was more successful in terms of nanoparticles' content than the first methodology, and thus, is the one selected for the next steps.

The characterization of the Cell/AuNPs, Cell/PtNPs and Cell/Fe_3O_4NPs single nanohybrids (prepared via the *in situ* synthesis of the corresponding NPs in the presence of cellulose microspheres) was performed by SEM coupled with energy dispersive X-ray spectroscopy

(EDS). According to the SEM micrographs (Fig. S7A), the size and shape of the cellulose microspheres were not affected by the functionalization with the individual inorganic nanoparticles (AuNPs, PtNPs and Fe_3O_4NPs).

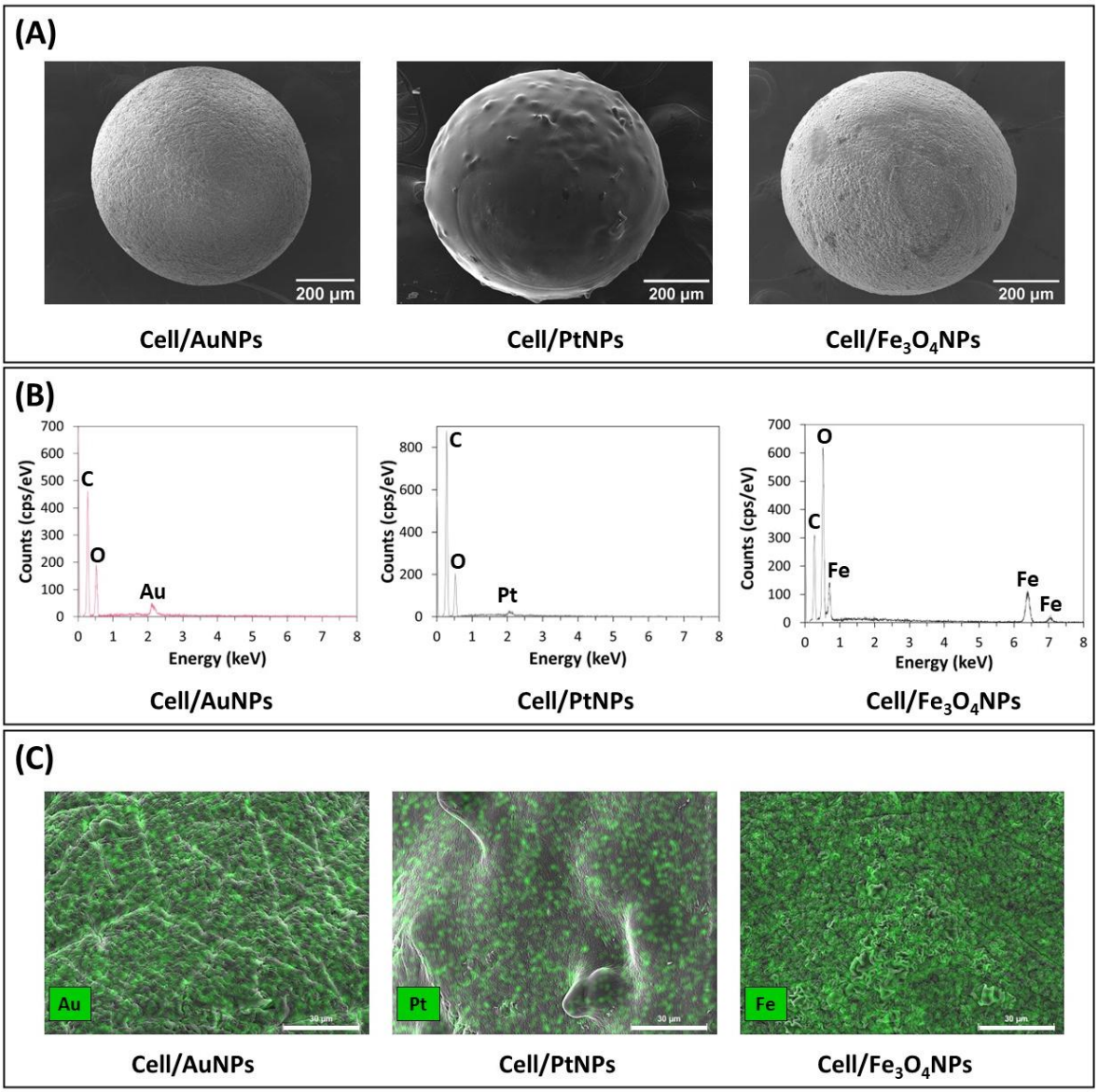

Fig. S7. (**A**) SEM micrographs, (**B**) EDS spectra and (**C**) SEM/EDS mapping of Au, Pt and Fe elements (scale bar: 30 µm) of the Cell/AuNPs, Cell/PtNPs and Cell/Fe_3O_4NPs prepared via the *in situ* synthesis of the corresponding NPs in the presence of the cellulose microspheres.

Furthermore, the EDS spectra (Fig. S7B) show that, apart from the carbon (C) and oxygen (O) peaks at 0.27 and 0.53 keV [10], respectively, the single nanohybrids present the corresponding peaks of gold (Au) at 2.12 keV [11], platinum (Pt) at 2.05 keV [12], and iron (Fe)

peaks at 0.71, 6.40 and 7.07 keV [12]. Table S2 shows the normalized element composition (wt.%, C, O, Au, Pt and Fe) of the single nanohybrids.

Table S2. EDS normalized element composition (C, O, Au, Pt and Fe) of the single nanohybrids.

	C (wt.%)	**O (wt.%)**	**Au (wt.%)**	**Pt (wt.%)**	**Fe (wt.%)**
Cell/AuNPs	46.2±17.2	51.0±19.3	2.8±0.5	–	–
Cell/PtNPs	47.3±17.5	52.2±19.7	–	0.50±0.16	–
Cell/Fe_3O_4NPs	23.1±13.5	41.6±21.5	–	–	35.5±4.6

The surface chemical composition of the Cell/AuNPs, Cell/PtNPs and Cell/Fe_3O_4NPs single nanohybrids was also checked by EDS mapping for gold, platinum and iron. As illustrated in Fig. S7C, each element is uniformly distributed across the corresponding single nanohybrids, which is consistent with the EDS spectral data (Fig. S7B).

The XRD diffractograms (Fig. S8A) of the Cell/AuNPs, Cell/PtNPs and Cell/Fe_3O_4NPs single nanohybrids display the characteristic broad peak of regenerated cellulose ($2\theta \approx 20°$ and 21° [13]), particularly in the samples with lower inorganic NPs content, such as Cell/AuNPs and Cell/PtNPs. Additionally, the diffractogram of the Cell/Fe_3O_4NPs nanohybrid exhibits distinct peaks corresponding to magnetite ($2\theta \approx 30°$, 36°, 43°, 53°, 57°, and 62° [14]), alongside the cellulose II diffraction pattern.

The thermogravimetric analysis (TGA, Fig. S8B) of the single nanohybrids show a one-step mass-loss degradation profile in the range of 240-380 °C with maximum decomposition temperatures of 336 °C for Cell/AuNPs, 332 °C for Cell/PtNPs and 321 °C for Cell/Fe_3O_4NPs. The total mass loss at 800 °C reached values of ca. 79% for Cell/AuNPs, 77% for Cell/PtNPs and 72% for Cell/Fe_3O_4NPs.

As anticipated, the Cell/PtNPs nanohybrid has the ability to randomly move (in-place rotation) in a medium containing H_2O_2 as fuel, contrary to the Cell/AuNPs and Cell/Fe_3O_4NPs nanohybrids that remained static under the tested conditions.

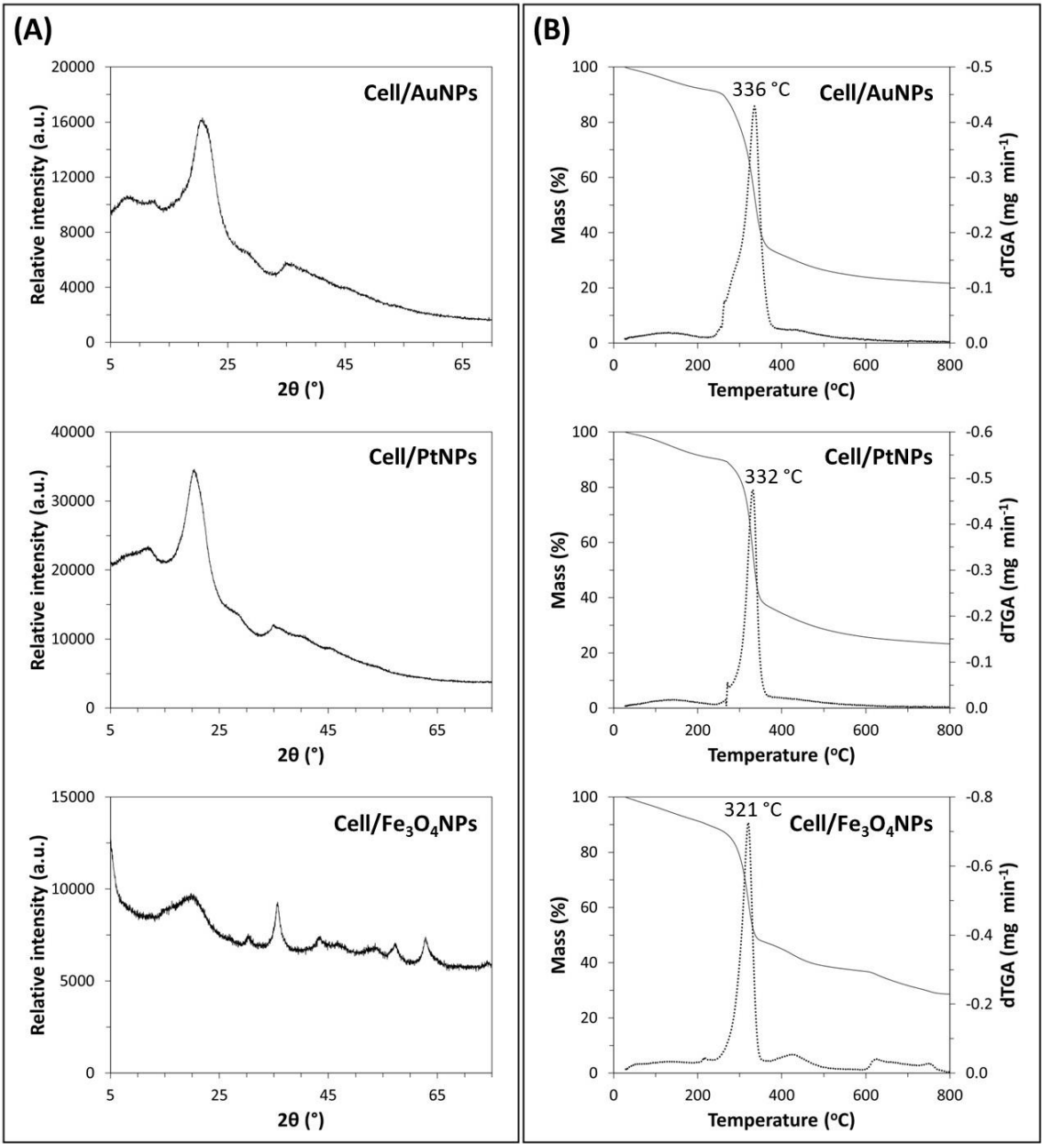

Fig. S8. (**A**) XRD diffractograms and (**B**) TGA thermograms (inert atmosphere) of the Cell/AuNPs, Cell/PtNPs and Cell/Fe_3O_4NPs prepared via the *in situ* synthesis of the corresponding NPs in the presence of cellulose microspheres.

The topography of the Cell/Fe_3O_4NPs single nanohybrid was analyzed by AFM. According to Fig. S9A, the single hybrid exhibited a low surface roughness with a S_a (arithmetical mean height of the surface) value at the nanoscale (ca. 73 nm), which is higher than the S_a value of the unfunctionalized cellulose microspheres (ca. 65 nm). The MFM phase analysis does not clearly confirm the magnetic behavior of Cell/Fe_3O_4NPs given the very low variation in contrast (Fig. S9B). Nevertheless, the Cell/Fe_3O_4NPs nanohybrid is capable of a magnetic

response in the presence of a magnet as undoubtedly observed in the time-lapse images in Fig. S9B. The Cell/AuNPs and Cell/PtNPs nanohybrids did not exhibit any magnetic response when exposed to a magnet.

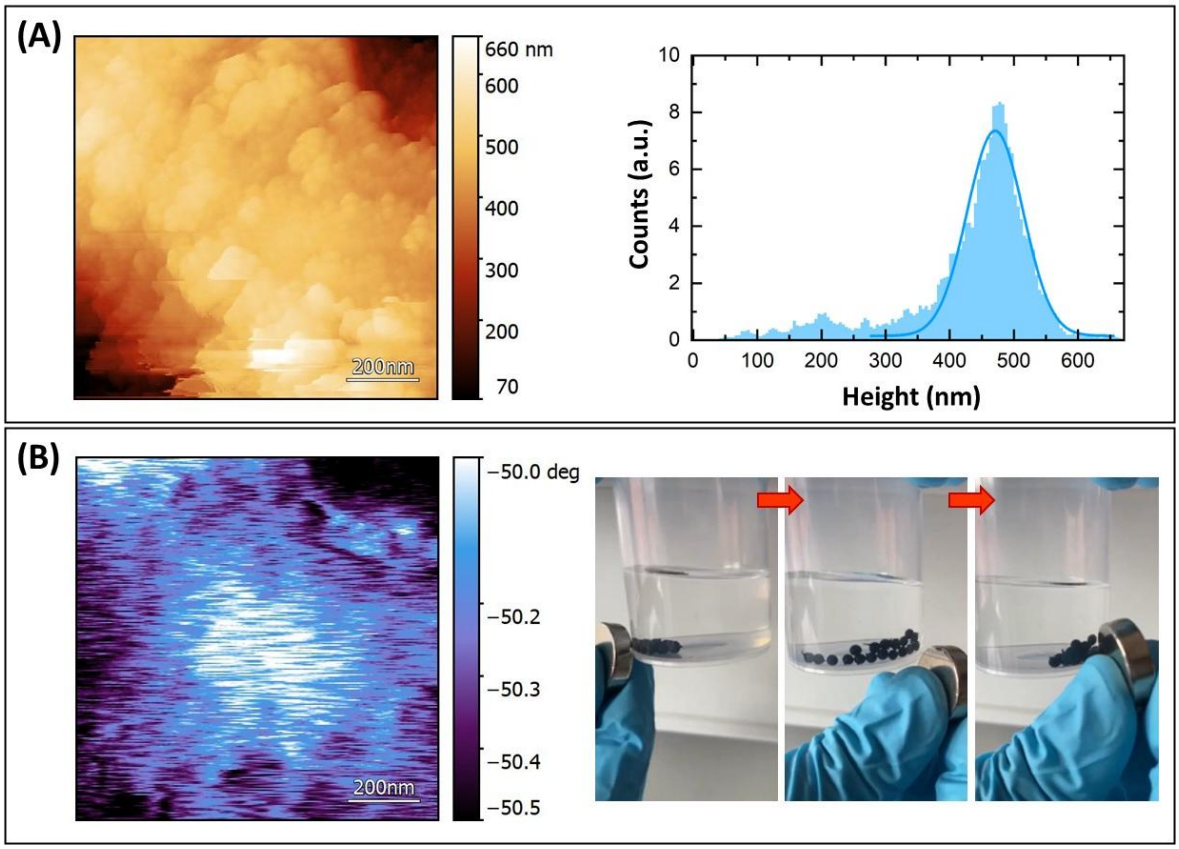

Fig. S9. (**A**) Atomic force micrograph and roughness analysis of the Cell/Fe_3O_4NPs single nanohybrid, and (**B**) magnetic force micrograph and photographs of the magnetic response of the Cell/Fe_3O_4NPs single nanohybrid after exposure to a magnet.

IV. Characterization techniques

IV.1. Rheology measurements

Rheology measurements were carried out with a Malvern Kinexus Lab+ Rheometer (Malvern Instruments, Malvern, United Kingdom) equipped with a Peltier element for temperature control, and a plat-plate geometry with a diameter of 40 mm, using a water lock to prevent dehydration of the samples. The shear viscosity of the cellulose solutions was evaluated as a function of shear rate at 27 °C by steady shear measurements, with shear rates ranging from 0.01–100 s^{-1}. Elastic (*G*') and viscous (*G*'') moduli were determined by an oscillatory frequency sweep test at 27 °C with as frequency sweep range of 0.01–10 Hz.

IV.2. Ultraviolet-visible (UV-Vis) spectroscopy

Absorption spectra were acquired with a Shimadzu UV1800 UV-vis spectrophotometer (Shimadzu Corporation, Kyoto, Japan) equipped with a quartz window plate with 10 mm diameter and the holder in the vertical position. The spectra were acquired in steps of 0.5 nm in the 300–700 nm range at room temperature.

IV.3. Transmission electron microscopy (TEM)

TEM micrographs were obtained by JEOL 2200 FS TEM microscope (GEOL, Tokyo, Japan) operating at 200 kV. The samples were prepared by placing a dispersion of nanoparticles onto a copper grid coated with a holey carbon film and allowing them to air-dry. The average size was determined with a minimum of 50 measurements using the Fiji image processing software.

IV.4. Dynamic light scattering (DLS)

Measurements of zeta potential were carried out in a Malvern Zetasizer Nano ZS equipment (Malvern Panalytical, Cambridge, United Kingdom), using ultrapure water as dispersion medium at room temperature. All test specimens were analyzed in triplicate (based on one hundred measurements per test specimens).

V. References

[1] R.J.B. Pinto, D. Bispo, C. Vilela, A.M.P. Botas, R.A.S. Ferrreira, A.C. Menezes, F. Campos, H. Oliveira, M.H. Abreu, S.A.O. Santos, C.S.R. Freire, One-minute synthesis of size-controlled fucoidan-gold nanosystems: antitumoral activity and dark field imaging, Materials (Basel). 13 (2020) 1076. https://doi.org/10.3390/ma13051076.

[2] W. Wu, S.-B. He, H.-P. Peng, H.-H. Deng, A.-L. Liu, X.-H. Lin, X.-H. Xia, W. Chen, Citrate-Capped Platinum Nanoparticle as a Smart Probe for Ultrasensitive Mercury Sensing, Anal. Chem. 86 (2014) 10955−10960. https://doi.org/10.1021/ac503544w.

[3] I. Alfaro, L. Molina, P. González, J. Gaete, F. Valenzuela, J.F. Marco, C. Sáez, C. Basualto, Silica-coated magnetite nanoparticles functionalized with betaine and their use as an adsorbent for Mo(VI) and Re(VII) species from acidic aqueous solutions, J. Ind. Eng. Chem. 78 (2019) 271–283. https://doi.org/10.1016/j.jiec.2019.06.002.

[4] M.A. Dheyab, A.A. Aziz, M.S. Jameel, O.A. Noqta, P.M. Khaniabadi, B. Mehrdel, Excellent relaxivity and X-ray attenuation combo properties of Fe3O4@Au CSNPs produced via Rapid sonochemical synthesis for MRI and CT imaging, Mater. Today Commun. 25 (2020) 101368. https://doi.org/10.1016/j.mtcomm.2020.101368.

[5] X. Huang, M.A. El-Sayed, Gold nanoparticles: Optical properties and implementations in cancer diagnosis and photothermal therapy, J. Adv. Res. 1 (2010) 13–28. https://doi.org/10.1016/j.jare.2010.02.002.

[6] R.P. Charde, B. van Devener, M.M. Nigra, Surfactant- and Ligand-Free Synthesis of Platinum Nanoparticles in Aqueous Solution for Catalytic Applications, Catalysts 13 (2023) 246. https://doi.org/10.3390/catal13020246.

[7] C. Devi, P. Kalita, D. Choudhury, M. Barthakur, Preparation and characterization of gold nanoparticles conjugated insulin, in: S. Paul, D. Bhatia (Eds.), Smart Healthc. Dis. Diagnosis Prev., Elsevier Inc., 2020: pp. 29–32. https://doi.org/10.1016/B978-0-12-817913-0.00005-5.

[8] B. Beyribey, B. Çorbacioğlu, Z. Altin, Synthesis of platinum particles from H2PtCl6 with hydrazine as reducing agent, Gazi Univ. J. Sci. 22 (2009) 351–357. https://dergipark.org.tr/tr/download/article-file/83059.

[9] P. Duel, M.N. Piña, J. Morey, One-Pot Environmentally Friendly Synthesis of Nanomaterials Based on Phytate-Coated Fe3O4 Nanoparticles for Efficient Removal of the Radioactive Metal Ions 90Sr, 90Y and (UO2)2+ from Water, Nanomaterials 12 (2022) 4383. https://doi.org/10.3390/nano12244383.

[10] C. Vilela, A.C.Q. Silva, E.M. Domingues, G. Gonçalves, M.A. Martins, F.M.L. Figueiredo, S.A.O. Santos, C.S.R. Freire, Conductive polysaccharides-based proton-exchange membranes for fuel cell applications: the case of bacterial cellulose and fucoidan, Carbohydr. Polym. 230 (2020) 115604. https://doi.org/10.1016/j.carbpol.2019.115604.

[11] P. Anbu, S.C.B. Gopinath, S. Jayanthi, Synthesis of gold nanoparticles using Platycodon grandiflorum extract and its antipathogenic activity under optimal conditions, Nanomater. Nanotechnol. 10 (2020) 1–9. https://doi.org/10.1177/1847980420961697.

[12] S. Lee, C. Yim, S. Jeon, Direct synthesis of platinum nanodots in ZIF-8/Fe3O4 core-shell hybrid nanoparticles, RSC Adv. 7 (2017) 31239–31243. https://doi.org/10.1039/c7ra04711h.

[13] F.S. Matos, S. Fateixa, N. von Weymarn, C.S.R. Freire, A.J.D. Silvestre, C. Vilela, Functional Fibers from Regenerated Wood Pulp Cellulose and a Natural-based Phytate with Enhanced Flame Retardancy Properties, J. Appl. Polym. Sci. 140 (2023) e54326. https://doi.org/10.1002/app.54326.

[14] X. Luo, X. Lei, N. Cai, X. Xie, Y. Xue, F. Yu, Removal of Heavy Metal Ions from Water by Magnetic Cellulose- Based Beads with Embedded Chemically Modified Magnetite Nanoparticles and Activated Carbon, ACS Sustain. Chem. Eng. 4 (2016) 3960−3969. https://doi.org/10.1021/acssuschemeng.6b00790.